Medical Sciences

Variability in Quantitative DCE-MRI: Sources and Solutions

Harrison Kim

Department of Radiology, University of Alabama at Birmingham, Birmingham, AL, USA

DCE-MRI has been extensively used for diagnosis, prognosis and therapy monitoring of various diseases including cancer. However, it has been reported that the perfusion parameters measured by DCE-MRI largely vary across different research sites, preventing data comparison in multi-institutional clinical trials. Recently, novel perfusion phantoms have been developed to correct scanner-driven errors, enabling quality assurance of quantitative DCE-MRI measurement. However, the sources for the variability in quantitating perfusion parameters are not only MRI scanners but also software packages and imaging protocols set by the operators. In this manuscript, the various sources influencing the variability in quantitative DCE-MRI measurement are reviewed, and the proper solutions to minimize those are discussed.

DCE-MRI | Pharmacokinetic analysis | Phantom

Introduction

Dynamic contrast-enhanced magnetic resonance imaging (DCE-MRI) is a noninvasive and nonionizing method for micro-vascular perfusion assessment by monitoring the dynamic change of MRI contrast agent in a target tissue (1-4). As vascular abnormality is one of the primary features of malignant tumors, DCE-MRI has been extensively evaluated for cancer diagnosis (5-7), prognosis (8-10), and therapy monitoring (11-16). However, quantitating perfusion parameters varies across different MRI scanners and software packages (17-21). Bane *et al* recently reported that the reproducibility coefficient (RDC) in measuring T1 values of a static phantom across ten different scanners was up to 23%, when the data were analyzed using a single software package (21). Similarly, the RDC in quantitating K^{trans} (wash-in rate) of various abdominal tissues across two different 3T MRI scanners was about 25% in our recent study (22), when the same imaging protocol, software package and operator were employed. Haye *et al* reported that the reproducibility in DCE-MRI measurement of 15 patients across four commercially available software packages was up to 74 % (18), when assessed by within-subject coefficient of variation. Due to these variations, DCE-MRI has been largely analyzed only qualitatively in routine clinical practice.

Accurate quantitative measurement of perfusion parameters by DCE-MRI will significantly impact the clinical care of cancer patients. The improved risk stratification and therapy assessment by quantitative DCE-MRI will lead to better treatment decisions and consequentially will result in more favorable clinical outcomes. Inaccurate estimation of tumor aggressiveness may lead to overtreatment engaged with unnecessary side effects or insufficient treatment which may cause the disease progression. Quantification of absolute perfusion parameters will also enable data comparison across different research cites, and thereby will facilitate collaboration among the institutes to develop advanced treatments. Image data quantification will ultimately enable automated clinical decisions, and with appropriate review, will reduce turnaround time leading to rapid determination of the optimal treatment for each patient.

Table 1 summarizes the sources of variability in quantitative DCE-MRI and the suggested solutions to minimize those. There are three major sources of variability in quantitative DCE-MRI such as MRI scanner, post image-processing software and operator. Each MRI scanner has unique hardware configuration, performing with vendor-specific pulse sequences and reconstruction schemes, which induces variation in quantitating T1 values, contrast concentration and perfusion parameters across different MRI scanners. The image processing and analysis schemes in a software package are not typically optimized for reliable quantitative DCE-MRI. The variation in imaging parameters and contrast agent determined by the operator may also induce variation in perfusion parameters. This manuscript reviews the factors causing the variability in quantitative DCE-MRI and the methods that have been proposed to reduce those.

Scanner dependent variables

Pulse sequence and Reconstruction algorithm

Quantitative Imaging Biomarkers Alliance (QIBA) suggests using 3D fast spoiled gradient echo (FSPGR) sequence for quantitative DCE-MRI (23). However, FSPGR sequence is not standardized across vendors, and moreover, each vendor provides several FSPGR sequences. For example, GE scanners provide LAVA, VIBRANT, FAME, FMPSPGR, and FSPGR, while SIEMENS scanners provide TurboFLASH and VIBE. A unique reconstruction algorithm optimized for each sequence is installed in the scanner and automatically implemented. As the details of acquisition sequences are not publically revealed, it is difficult to fully comprehend the differences among them and thereby hard to predict how MRI signal will vary accordingly.

One approach for reducing scanner dependent variation is to use external phantoms with known contrast concentrations. A look-up table (LUT) to correlate between the true values of phantoms and the measured ones by MRI can be created and used to compensate the variation in quantitating contrast concentration across different sequences. QIBA developed a static phantom composed of 32 spheres having different T1 values (24), which was used to test the repeatability of DCE-MRI measurement of prostate cancer in a multi-cite clinical trial, ACRIN6701 (25). A similar static phantom was manufactured by the National Institute of Standards and Technology (NIST) (26), and used to determine the repeatability in quantitating various T1 values across multiple MRI scanners (1.5T or 3.0T) in eight institutes (21). These phantoms are now commercially available by several vendors including Phantom Laboratory, Inc (Salem, NY) (27) and High Precision Devices, Inc (Boulder, CO) (28).

Conflict of Interest: No conflicts declared.
Corresponding Author: Harrison Kim.
Department of Radiology
University of Alabama at Birmingham,
VH G082C5, 1670 University Boulevard,
Birmingham, AL 35294-0012, USA
Phone: 205-996-4088; Fax: 205-975-6522.
E-mail: hyunki@uab.edu.

Table 1. Variables in quantitative DCE-MRI. Major sources and variables in quantitative DCE-MRI are listed together with suggested solutions.

Source	Variable	Solution
Scanner	Pulse sequence and reconstruction algorithm	Phantom-based scanner calibration
	B1 non-uniformity	B1 shimming and mapping
Software	Image co-registration	Optimization of image co-registration method
	Arterial input function (AIF)	Optimization of AIF determination method
	Pharmacokinetic (PK) model	Use of the same PK model
	Software bugs	Validation of the software package using DROs
Operator	Imaging parameters	Use of the same imaging parameters & Phantom-based scanner calibration
	Contrast agent	Use of the same contrast agent

However, a static phantom may not be ideal to model dynamically changing contrast concentration in live tissues, because: **a)** the movement of contrast agents *in vivo* causes additional signal reduction not captured by static phantoms, **b)** the number of spheres in a static phantom is limited, thus may induce larger fitting errors in the estimation of a LUT, **c)** B1 mapping techniques are usually T1 dependent, leading to the flip-angle miscalculation on a static phantom, especially in high field MRI (≥3T) (29-32). Therefore, a perfusion phantom varying its contrast concentration would be necessary. Most MRI perfusion phantoms developed for system calibration are operated by programmable syringe pumps, varying the mixing ratio between water and contrast agent in plastic hollow spheres (33-35). Since MRI measurement with the same sequence may also vary over time due to hardware instability (36), the LUT obtained from a phantom should be updated periodically. However, the optimal frequency for LUT update is unknown and may be different according to scanners. Therefore ideally, the phantom should be imaged together with a human subject to obtain the LUT at every imaging. But most phantoms are too bulky to be imaged with a human subject simultaneously.

We recently developed a portable perfusion phantom that can be imaged concurrently with a human subject for real-time quality assurance (22). The phantom is readily operable by typical MRI technologists in routine clinical settings, and made of inexpensive material so that it can be manufactured as a disposable device. Figure 1A shows the photograph of the phantom (width x height x length = 24 x 23 x 208 mm). Three phantoms are used in a phantom package as shown in Fig. 1B, not only to increase the signal-to-noise ratio (SNR) of measurement but to detect any functional error if occurs in one of the phantoms. The phantoms are surrounded by thermal insulation material (polyurethane) to prevent heat transfer from a patient. Figure 1C shows MRI image of a patient and three phantoms at about 8 minutes after contrast injection. The phantom package is located at the bottom of a patient during imaging. Figure 1D shows the CECs of three phantoms and the mean value when contrast was injected at 15 seconds after imaging start. The main concern of this approach is that the space within the scanner is reduced by the phantom package. The phantom package and fiberglass cushion placed on the top of it requires about 50 mm, which can be a concern for large and/or claustrophobic patients. If the proper frequency for LUT update is known, the portable perfusion phantom will be able to be used with slim and non-claustrophobic patients once in a while.

B1 field non-uniformity

B1 field generated by a bird-cage RF body coil is highly uniform in the air (37), but perturbed by a human subject present within the coil primarily due to the tissue permittivity varying across the body region (38). B1 field strength is linearly proportional to the flip angle (FA), thus B1 field non-uniformity results in FA variation over the body, which leads to error in quantification of T1 values and consequentially tissue contrast concentration and perfusion parameters. The variation of tissue permittivity increases in proportion to the main field (B0) strength and the body size, as that is affected by the wavelength of RF transmission field (39). In a lower field MRI (B0 ≤ 1.5T), the RF wavelength is typically larger than the size of human body, therefore the tissue permittivity induced by the RF interference is rather homogenous over the body region, leading to relatively uniform B1 field and FA values. However, in a higher field MRI (B0 ≥ 3.0T), the RF wavelength becomes smaller than the body size, thus the tissue permittivity variation becomes more evident according to the RF wave pattern propagating through the body. Most modern 3T MRI scanners are capable of multi-channel RF transmission, allowing more uniform B1 field (40). A multi-channel RF coil transmits two or more independent RF pulses with different magnitudes, phases and waveforms so that the uniformity of B1 field is optimized for each patient. This technique is referred to as B1 shimming. B1 shimming significantly improves B1 homogeneity, but B1 variation is still present to a certain extent depending upon the body size and composition (41). Therefore even after B1 shimming, it would be still necessary to measure B1 non-uniformity, which is referred to as B1 mapping.

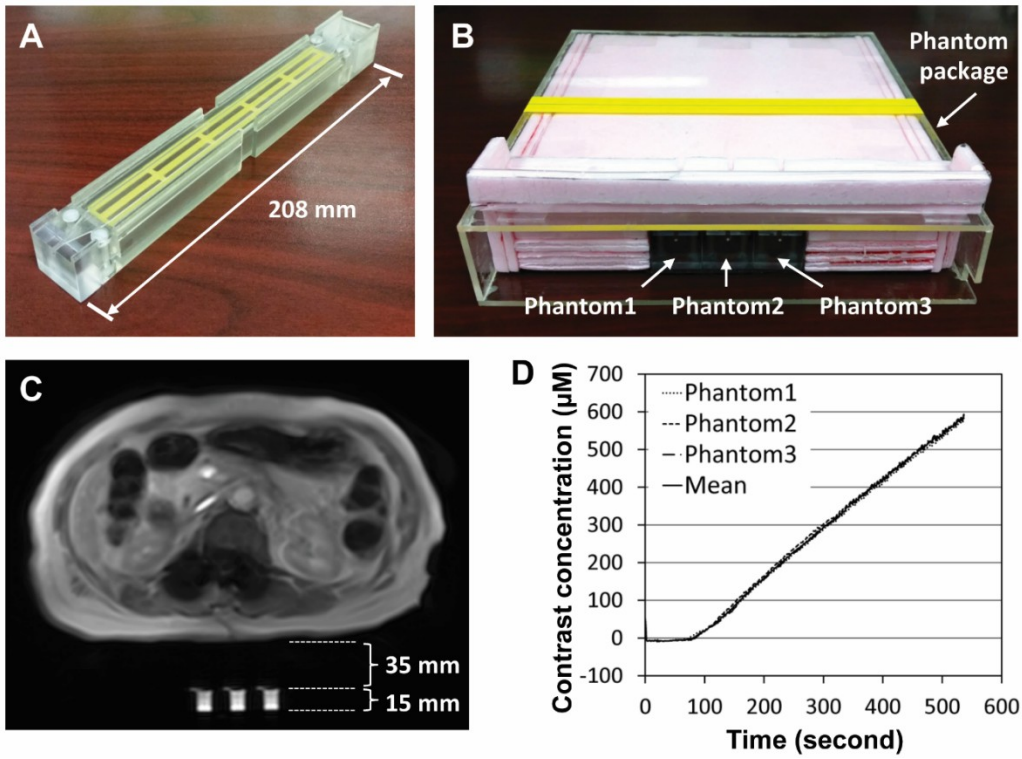

Figure 1. Novel portable perfusion phantom. (A, B) Photographs of (A) the portable perfusion phantom and (B) the phantom package containing three portable perfusion phantoms. (C) A representative DCE-MRI image of a patient and three phantoms located under the patient at about 8 minutes after dosing. (D) Contrast enhancement curves of three perfusion phantoms shown in Fig. 1C and the mean value.

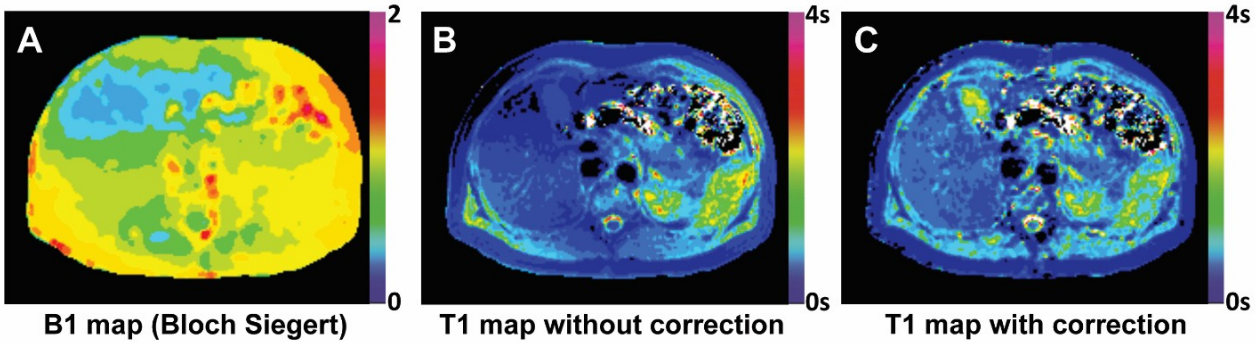

Figure 2. T1 map with or without B1 map correction. (A) B1 map of the abdomen created by Block Siegert method. (B, C) T1 map (B) with or (C) without correction using the B1 map shown in Fig. 2A.

To date, a number of B1 mapping techniques have been introduced (29-32, 42-46), and each vendor employs one of them. For instance, Block-Siegert method is used in GE scanners (44), preconditioning RF pulse based B1 mapping is used in SIEMENS scanners (45), and multiple TR B1/T1 mapping is used in PHILIPS scanners (46). Figure 2A shows a B1 map of the abdomen at a 3T GE scanner generated by Block-Siegert method, and Figs. 2B and 2C show T1 maps before and after B1 map correction, respectively.

Software dependent variables

Image co-registration

In DCE-MRI, accurate image co-registration is critical to generate a reliable CEC, which is directly related to the accuracy in perfusion parameter quantification. Typically, 50~200 images are acquired during DCE-MRI, so it is impractical to register all images manually. Two approaches are generally used for automatic image co-registration in DCE-MRI such as rigid and non-rigid methods (47). Rigid image co-registration is to match images of a moving object into a reference image via translation and rotation without changing the distance between any two pixels in each image. Rigid image co-registration is appropriate for regions whose tissues are fixed in position such as brain, breast and prostate. In non-rigid image co-registration, however, the distance between two pixels is not preserved during process, thus it is commonly employed for DCE-MRI of the abdomen whose internal organs move in coordination with breathing and peristalsis. For improved performance of image co-registration in abdominal DCE-MRI, only the images acquired at the expiration phase can be retrospectively selected and then used for image co-registration (48). The executable files and source codes for various image co-registration schemes are freely available from the elastix website (49), but the detail co-registration parameters should be adjusted for optimal performance in each application.

Arterial input function

Arterial input function (AIF) is the dynamic change of contrast concentration in artery following intravenous bolus injection of contrast agent (50). Since the microvascular perfusion in a tissue is defined as the flow of contrast agent between the artery and tissue, the accurate determination of AIF is essential to quantitate perfusion parameters in DCE-MRI (51-53). If large feeding arteries are present near the target region within the FOV, the AIF can be directly measured from the arterial regions. However there are a few concerns in direct AIF measurement. First, the arterial blood may not be fully saturated, leading to AIF overestimation (54, 55). Thus the AIF should be retrieved from the artery in the image slice located at least 30 mm away from the first slice when the blood flows from the first slice toward the second one (56). Second, error in MRI signal is amplified during AIF quantification in proportional to contrast concentration due to the nonlinear relationship between MRI signal and contrast concentration (57); this is the primary reason why AIF is often unreliable in the first passage. Third, blood flow pulsatility may allow unsaturated blood to enter the image slice intermittently, causing spike noise in AIF. Unless severe, it may be readily removed using median filtering after the second peak, but it may not be during the first passage. This is another reason why the first peak of AIF can be unreliable. Fourth, AIF may be underestimated in high-field MRI owing to T2* effect induced by contrast agent. In general, contrast concentration is calculated under the assumption that T2* is at least ten fold larger than echo time (58). T2* decreases in proportional to both the contrast concentration and magnetic field strength. Therefore T2* effect by contrast agent becomes more evident in high-field MRI, leading to AIF underestimation especially during the first passage. Fifth, MRI signal at the boundary of the arterial region may be influenced by partial volume effect, leading to AIF underestimation. We have shown that AIF can vary up to 15% according to the size of the region-of-interest (ROI) (59). Thus the boundary of the arterial region should be excluded in determining AIF, while the boundary thickness should be larger than the pixel size. Lastly, the temporal resolution should be sufficiently high (ideally 1~2 seconds) to prevent AIF underestimation during the first passage.

Several alternative methods have been proposed, when AIF cannot be directly measured. A population-based AIF (pAIF) is the average of AIFs directly measured from the arteries of many human subjects (60-62). A pAIF has high SNR, but cannot incorporate variation across the individuals. Besides, a pAIF may also vary according to artery location, contrast agent, dose amount, infusion rate and magnetic field strength. Reference region model (RRM) is to quantitate perfusion parameters using the dynamic change of contrast concentration in a reference tissue to eliminate the need of AIF (63-65). RRM assumes that the fractional extravascular extracellular volume (EEV) of the reference region is consistent across the subjects. Muscle was commonly chosen for the reference region, but the EEV of paravertebral muscle varied about 35% among five male rats (~350 g), leading to significant variability in quantitating perfusion parameters (63). The variability may be even severer among patients in clinical practice due to the variation in age, gender, race and disease status. Multiple reference tissue model (MRTM) uses two or more reference tissues (66, 67). MRTM estimates perfusion parameters of multiple reference tissues via iterative process and in turn, retrieves an AIF for each tissue. MRTM, however, yielded perfusion parameters with similar reproducibility to those by a pAIF (66).

We have recently proposed a new method to combine the merits of both the directly measured AIF (mAIF) and pAIF (68). The AIF variation across the individuals mainly stems from the variation in cardiac output and blood volume. The higher cardiac output results in the sharper AIF, while the higher blood volume leads to the lower amplitude of AIF. Thus the individual variation in cardiac output can be estimated by the full width at half maximum (FWHM) of AIF during the first passage, and that in the blood volume (or dose amount) can be estimated by the AIF amplitude. Therefore a high SNR AIF incorporating the individual variations can be obtained by scaling the pAIF in time to match its FWHM with that of a mAIF and then adjust its amplitude to fit into that of the mAIF; in amplitude fitting, the mAIF during the first passage is not included due to its uncertainty. This method heavily relies on the quality of the pAIF under the assumption that the cardiac output does not change during DCE-MRI.

Pharmacokinetic modeling

Perfusion parameters will vary according to pharmacokinetic (PK) models, thus it is necessary to employ the same PK model for data comparison in a multi-site clinical trial. In general, three PK models have been utilized to quantitate perfusion parameters in DCE-MRI such as Tofts model (TM) (69), extended Tofts model (ETM) (70), and Shutter-speed model (SSM) (71). TM, ETM, and SSM are expressed by equations 1-3, respectively.

$$C_t(t) = K^{trans}\int_0^t C_p(t')dt' - k_{ep}\int_0^t C_t(t')dt' \quad (1)$$

$$C_t(t) = v_p C_p(t) + K^{trans}(1+\frac{v_p}{v_e})\int_0^t C_p(t')dt' - \frac{K^{trans}}{v_e}\int_0^t C_t(t')dt' \quad (2)$$

$$R_1(t) = \frac{1}{2}[\{2R_{1i} + r_1\frac{K^{trans}}{v_e}\int_0^t C_p(t')\exp(-\frac{K^{trans}}{v_e}(t-t'))dt' + (R_{10} - R_{1i} + \frac{1}{\tau_i})/v_e\} - \{[\frac{2}{\tau_i} + (R_{10} - R_{1i} - \frac{1}{\tau_i})/v_e - r_1\frac{K^{trans}}{v_e}\int_0^t C_p(t')\exp(-\frac{K^{trans}}{v_e}(t-t'))dt']^2 + 4\frac{(1-v_e)}{\tau_i^2 v_e}\}^{1/2}] \quad (3)$$

, where $C_t(t)$ is tissue contrast concentration at time t, $C_p(t)$ is contrast concentration in the arterial plasma at time t, $R_1(t)$ is the tissue apparent longitudinal relaxation rate constant at time t, R_{1i} is the intracellular longitudinal relaxation rate constant, R_{10} is the pre-contrast tissue longitudinal relaxation rate constant, and r_1 is the tissue contrast relaxivity. Perfusion parameters are K^{trans} (forward volume transfer constant: Wash-in rate), k_{ep} (reverse reflex rate constant: Washout rate), v_p (fractional plasma volume), v_e (fractional extravascular extracellular volume: $v_e = K^{trans}/k_{ep}$) and τ_i (mean intracellular water molecule lifetime). $C_p(t)$ is called plasma input function (PIF), which is AIF divided by (1–hematocrit), thus for each patient, hematocrit must be measured to determine $C_p(t)$ accurately. Contrast concentration is calculated by

$$C = \frac{1}{r_1}\left\{\frac{1}{TR}\ln\left(\frac{M_0\sin\theta - S\cos\theta}{M_0\sin\theta - S}\right) - \frac{1}{T_1(0)}\right\} \quad (4)$$

, where r_1 is tissue contrast relaxivity, TR is repetition time, $T_1(0)$ is pre-contrast T1 value, S is the measured MRI signal, M_0 is the original magnetization and θ is a flip angle.

Either TM or ETM is a two-compartmental model (intravascular space *vs* extracellular-extravascular space), while SSM is a three-compartmental model (intravascular space, extracellular-extravascular space, and intracellular-extravascular space) (53). TM or ETM assumes water exchange between cells and extracellular space is infinitely fast, whereas SSM does not, thus TM or ETM tends to underestimate tissue perfusion parameters in comparison to SSM (17). It has been reported that SSM allows more accurate measurement (72, 73), but SSM is less popular as it is a relatively new approach. TM assumes that the fractional plasma volume is inconsequential. The vascular volume in a regular tissue is about 5% (74), but it varies according to tissues and disease types. Therefore ETM may provide more accurate perfusion parameters than TM, but due to mathematical simplicity, TM is also commonly used.

Software bugs

Quantitative DCE-MRI software packages must be validated prior to use with digital reference objects (DROs), synthetic image data made for software validation (75, 76). However, most in-house (or commercial) software packages are not validated, so often generate huge computational error. Huang *et al* reported significant variation in perfusion parameters among six software packages, when the same PK model, T1 map, AIF, and ROI were used (17), and similar results were reported by Heye *et al* (18) and Kudo *et al* (19). Dr. Barboriak and QIBA developed DROs to validate software packages quantifying DCE-MRI perfusion parameters (77). The DROs provide AIF and various CECs, yielding different perfusion parameters when TM or ETM is employed. But to date, DROs for SSM have not been developed. DROs that validate the software packages for T1 mapping, contrast-concentration mapping and AIF determination will need to be developed as well.

Operator dependent variation

Imaging parameters

Imaging parameters determine four primary qualities of an image such as image contrast, spatial resolution, temporal resolution and SNR; generally, one can be enhanced by sacrificing the others. In MRI, major imaging parameters include repetition time (TR), echo time (TE), flip angle (FA), field of view (FOV), frequency/phase encoding, slice number, number of excitation (NEX) and acceleration factor. TR, TE and FA determine image contrast and temporal resolution. FOV, frequency/phase encoding and slice number determine spatial and temporal resolutions. NEX and acceleration factor determine temporal resolution and SNR. Imaging parameters should be optimized for each target region, as suggested by QIBA (23). However, since each MRI scanner is equipped with vendor-specific and model-specific settings of imaging parameters, it is difficult to apply the same imaging parameters across different MRI scanners, which may lead to variability in quantitating perfusion parameters. Therefore it would be necessary to set up the imaging parameters as close to the ones standardized by QIBA as possible, and then calibrate MRI scanners with a perfusion phantom to detect and compensate the variability that may be induced by different imaging parameters.

Contrast agent

Gadolinium (Gd) based MRI contrast agents have unique relaxivities (78), which may influence the perfusion-parameter quantification. The relaxivity is inversely proportional to the quantitated value of contrast concentration (see Eq. 4), and varies according to temperature, magnetic-field strength and the substance that the contrast agent is dissolved in. If the relaxivity of a contrast agent in the arterial plasma is consistent with that in a target tissue, those are cancelled out in TM or ETM without influencing the perfusion-parameter quantification (see Eqs. 1 and 2). The relaxivity of a contrast agent is commonly assumed to be consistent regardless of tissues for mathematical simplicity. But the relaxivity is not necessarily consistent across the tissues (79), and the magnitude of relaxivity variation across the tissues may be dependent upon the contrast agent. Besides, Gd-based contrast agents have unique viscosities (80), which may also influence the micro-vascular perfusion. Therefore it would be important to use the same contrast agent for data comparison in a multi-site clinical trial.

Conclusion

To date, quantitative DCE-MRI has been often considered impractical due to many variables affecting perfusion-parameter quantification. However, recent progress in developing reliable perfusion phantoms for system calibration and novel image-processing schemes together with QIBA's endeavor to standardize the imaging protocol has allowed accurate tissue-perfusion assessment using DCE-MRI. For its routine and global use, however, the perfusion phantoms should be readily operable by a typical technologist and ideally disposable. Besides, the software package will need to be implemented automatically to minimize the operator-dependent bias and to improve the operation speed for quick turnaround time. Accurate quantitative DCE-MRI will ultimately allow automated computer aided diagnosis, prognosis, and therapy monitoring, which will significantly improve the clinical outcomes for cancer patients.

Acknowledgement

Financial support for this work: NIH, Bethesda, MD, USA, Grant 5P30CA013148 and Research Initiative Pilot Award from the Department of Radiology at UAB.

1. Barnes SL, Whisenant JG, Loveless ME, Yankeelov TE. 2012. Practical dynamic contrast enhanced MRI in small animal models of cancer: data acquisition, data analysis, and interpretation. *Pharmaceutics*. 4:442-478.
2. Zhang CC, Yan Z, Giddabasappa A, Lappin PB, Painter CL, Zhang Q, Li G, Goodman J, Simmons B, Pascual B, Lee J, Levkoff T, Nichols T, Xie Z. 2014. Comparison of dynamic contrast-enhanced MR, ultrasound and optical imaging modalities to evaluate the antiangiogenic effect of PF-03084014 and sunitinib. *Cancer medicine*. 3:462-471.
3. Craciunescu OI, Blackwell KL, Jones EL, Macfall JR, Yu D, Vujaskovic Z, Wong TZ, Liotcheva V, Rosen EL, Prosnitz LR, Samulski TV, Dewhirst MW. 2009. DCE-MRI parameters have potential to predict response of locally advanced breast cancer patients to neoadjuvant chemotherapy and hyperthermia: a pilot study. *Int J Hyperthermia*. 25:405-415.
4. Kim H, Folks KD, Guo L, Sellers JC, Fineberg NS, Stockard CR, Grizzle WE, Buchsbaum DJ, Morgan DE, George JF, Zinn KR. 2011. Early therapy evaluation of combined cetuximab and irinotecan in orthotopic pancreatic tumor xenografts by dynamic contrast-enhanced magnetic resonance imaging. *Mol Imaging*. 10:153-167.
5. Tan CH, Hobbs BP, Wei W, Kundra V. 2015. Dynamic contrast-enhanced MRI for the detection of prostate cancer: meta-analysis. *AJR Am J Roentgenol*. 204:W439-448.
6. Turkbey B, Thomasson D, Pang Y, Bernardo M, Choyke PL. 2010. The role of dynamic contrast-enhanced MRI in cancer diagnosis and treatment. *Diagn Interv Radiol*. 16:186-192.
7. Turnbull LW. 2009. Dynamic contrast-enhanced MRI in the diagnosis and management of breast cancer. *NMR Biomed*. 22:28-39.
8. Arevalo-Perez J, Kebede AA, Peck KK, Diamond E, Holodny AI, Rosenblum M, Rubel J, Gaal J, Hatzoglou V. 2016. Dynamic contrast-enhanced MRI in low-grade versus anapestic oligodendrogliomas. *Journal of neuroimaging*. 26:366-371.
9. Wu J, Gong G, Cui Y, Li R. 2016. Intratumor partitioning and texture analysis of dynamic contrast-enhanced (DCE)-MRI identifies relevant tumor subregions to predict pathological response of breast cancer to neoadjuvant chemotherapy. *Journal of Magnetic Resonance Imaging*. 44:1107-1115.
10. Berman RM, Brown AM, Chang SD, Sankineni S, Kadakia M, Wood BJ, Pinto PA, Choyke PL, Turkbey B. 2016. DCE MRI of prostate cancer. *Abdominal Radiology*. 41:844-853.
11. Cheung YC, Chen SC, Su MY, See LC, Hsueh S, Chang HK, Lin YC, Tsai CS. 2003. Monitoring the size and response of locally advanced breast cancers to neoadjuvant chemotherapy (weekly paclitaxel and epirubicin) with serial enhanced MRI. *Breast Cancer Res Treat*. 78:51-58.
12. Martincich L, Montemurro F, De Rosa G, Marra V, Ponzone R, Cirillo S, Gatti M, Biglia N, Sarotto I, Sismondi P, Regge D, Aglietta M. 2004. Monitoring response to primary chemotherapy in breast cancer using dynamic contrast-enhanced magnetic resonance imaging. *Breast Cancer Res Treat*. 83:67-76.
13. Jia Q, Xu J, Jiang W, Zheng M, Wei M, Chen J, Wang L, Huan Y. 2013. Dynamic contrast-enhanced MR imaging in a phase study on neoadjuvant chemotherapy combining Rh-endostatin with docetaxel and epirubicin for locally advanced breast cancer. *International journal of medical sciences*. 10:110-118.
14. Hoskin PJ, Saunders MI, Goodchild K, Powell ME, Taylor NJ, Baddeley H. 1999. Dynamic contrast enhanced magnetic resonance scanning as a predictor of response to accelerated radiotherapy for advanced head and neck cancer. *The British journal of radiology*. 72:1093-1098.
15. Ceelen W, Smeets P, Backes W, Van Damme N, Boterberg T, Demetter P, Bouckenooghe I, De Visschere M, Peeters M, Pattyn P. 2006. Noninvasive monitoring of radiotherapy-induced microvascular changes using dynamic contrast enhanced magnetic resonance imaging (DCE-MRI) in a colorectal tumor model. *International journal of radiation oncology, biology, physics*. 64:1188-1196.
16. Ahn SJ, Koom WS, An CS, Lim JS, Lee SK, Suh JS, Song HT. 2012. Quantitative assessment of tumor responses after radiation therapy in a DLD-1 colon cancer mouse model using serial dynamic contrast-enhanced magnetic resonance imaging. *Yonsei medical journal*. 53:1147-1153.
17. Huang W, Li X, Chen Y, Chang MC, Oborski MJ, Malyarenko DI, Muzi M, Jajamovich GH, Fedorov A, Tudorica A, Gupta SN, Laymon CM, Marro KI, Dyvorne HA, Miller JV, Barbodiak DP, Chenevert TL, Yankeelov TE, Mountz JM, Kinahan PE, Kikinis R, Taouli B, Fennessy F, Kalpathy-Cramer J. 2014. Variations of dynamic contrast-enhanced magnetic resonance imaging in evaluation of breast cancer therapy response: a multicenter data analysis challenge. *Translational oncology*. 7:153-166.
18. Heye T, Davenport MS, Horvath JJ, Feuerlein S, Breault SR, Bashir MR, Merkle EM, Boll DT. 2013. Reproducibility of dynamic contrast-enhanced MR imaging. Part I. Perfusion characteristics in the female pelvis by using multiple computer-aided diagnosis perfusion analysis solutions. *Radiology*. 266:801-811.
19. Kudo K, Christensen S, Sasaki M, Ostergaard L, Shirato H, Ogasawara K, Wintermark M, Warach S. 2013. Accuracy and reliability assessment of CT and MR perfusion analysis software using a digital phantom. *Radiology*. 267:201-211.
20. Kim H, Arnoletti PJ, Christein J, Heslin MJ, Posey JA, 3rd, Pednekar A, Mark Beasley T, Morgan DE. 2014. Pancreatic adenocarcinoma: a pilot study of quantitative perfusion and diffusion-weighted breath-hold magnetic resonance imaging. *Abdominal imaging*. 39:744-752.
21. Bane O, Hectors SJ, Wagner M, Arlinghaus LL, Aryal MP, Cao Y, Chenevert TL, Fennessy F, Huang W, Hylton NM, Kalpathy-Cramer J, Keenan KE, Malyarenko DI, Mulkern RV, Newitt DC, Russek SE, Stupic KF, Tudorica A, Wilmes LJ, Yankeelov TE, Yen YF, Boss MA, Taouli B. 2017. Accuracy, repeatability, and interplatform reproducibility of T1 quantification methods used for DCE-MRI: Results from a multicenter phantom study. *Magn Reson Med*.
22. Kim H, Mousa M, Schexnailder P, Hergenrother R, Bolding M, Ntsikoussalabongui B, Thomas V, Morgan DE. 2017. Portable perfusion phantom for quantitative DCE-MRI of the abdomen. *Med Phys*. 44:5198-5209.
23. QIBA. 2012. Profile: DCE MRI Quantification]. Available from: http://www.rsna.org/uploadedFiles/RSNA/Content/Science_and_Education/QIBA/DCE-MRI_Quantification_Profile_v1%200-ReviewedDraft%208-8-12.pdf.
24. Jackson EF, Gupta SN, A. RM, Ashton EA, Karczmar GS, Evelhoch JL, Buonocore MH, Purdy DE, Zahlmann G. 2010. QIBA DCE-MRI technical committee update: phantom studies and first DCEMRI profile. *Proceedings of the 96th Scientific Assembly and Annual Meeting of the Radiological Society of North America, Chicago, Ill, USA, December 2010*.
25. Choi H. Repeatability assessment of quantitative DCE-MRI and DWI: a multi-center study of functional imaging standardization in the prostate.: https://www.mdanderson.org/patients-family/diagnosis-treatment/clinical-trials/clinical-trials-index/clinical-trials-detail.IDACRIN6701.html; [cited 2018 January 9].
26. Russek S. NIST phantoms. http://collaborate.nist.gov/mriphantoms/bin/view/MriPhantoms/PhantomOverview; [cited 2018 January 9].
27. Buonocore MH, Gultekin DH, Jacobs MA, Sammet S, Raghunand N, Levy J, Knopp MV. 2010. Design and testing of a phantom for calibration of MRI systems used in DCE-MRI clinical trials. *Proc Intl Soc Mag Reson Med*. 18.
28. Keenan KE, Wilmes LJ, Aliu SO, Newitt DC, Jones EF, Boss MA, Stupic KF, Russek SE, Hylton NM. 2016. Design of a breast phantom for quantitative MRI. *J Magn Reson Imaging*. 44:610-619.
29. Cunningham CH, Pauly JM, Nayak KS. 2006. Saturated double-angle method for rapid B1+ mapping. *Magnetic resonance in medicine*. 55:1326-1333.
30. Choi N, Lee J, Kim MO, Shin J, Kim DH. 2014. A modified multi-echo AFI for simultaneous B1(+) magnitude and phase mapping. *Magnetic resonance imaging*. 32:314-320.
31. Morrell GR. 2008. A phase-sensitive method of flip angle mapping. *Magnetic resonance in medicine*. 60:889-894.
32. Jiru F, Klose U. 2006. Fast 3D radiofrequency field mapping using echo-planar imaging. *Magnetic resonance in medicine*. 56:1375-1379.
33. Knight SP, Browne JE, Meaney JF, Smith DS, Fagan AJ. 2016. A novel anthropomorphic flow phantom for the quantitative evaluation of prostate DCE-MRI acquisition techniques. *Physics in Medicine and Biology*. 61:7466-7483.
34. Freed M, de Zwart JA, Hariharan P, Myers MR, Badano A. 2011. Development and characterization of a dynamic lesion phantom for

the quantitative evaluation of dynamic contrast-enhanced MRI. *Medical physics*. 38:5601-5611.
35. Chiribiri A, Schuster A, Ishida M, Hautvast G, Zarinabad N, Morton G, Otton J, Plein S, Breeuwer M, Batchelor P, Schaeffter T, Nagel E. 2013. Perfusion phantom: An efficient and reproducible method to simulate myocardial first-pass perfusion measurements with cardiovascular magnetic resonance. *Magn Reson Med*. 69:698-707.
36. O'Callaghan J, Wells J, Richardson S, Holmes H, Yu Y, Walker-Samuel S, Siow B, Lythgoe MF. 2014. Is your system calibrated? MRI gradient system calibration for pre-clinical, high-resolution imaging. *PLoS One*. 9:e96568.
37. Hayes CE, Edelstein WA, Schenck JF, Mueller OM, Eash M. 1985. An efficient, highly homogeneous radiofrequency coil for whole-body NMR imaging at 1.5 T. *Journal of Magnetic Resonance*. 63:622-628.
38. Gabriel C, Gabriel S, Corthout E. 1996. The dielectric properties of biological tissues: I. Literature survey. *Phys Med Biol*. 41:2231-2249.
39. Sled JG, Pike GB. 1998. Standing-wave and RF penetration artifacts caused by elliptic geometry: an electrodynamic analysis of MRI. *IEEE Trans Med Imaging*. 17:653-662.
40. Katscher U, Bornert P. 2006. Parallel RF transmission in MRI. *NMR in biomedicine*. 19:393-400.
41. Christ A, Kainz W, Hahn EG, Honegger K, Zefferer M, Neufeld E, Rascher W, Janka R, Bautz W, Chen J, Kiefer B, Schmitt P, Hollenbach HP, Shen J, Oberle M, Szczerba D, Kam A, Guag JW, Kuster N. 2010. The Virtual Family--development of surface-based anatomical models of two adults and two children for dosimetric simulations. *Phys Med Biol*. 55:N23-38.
42. Dowell NG, Tofts PS. 2007. Fast, accurate, and precise mapping of the RF field in vivo using the 180 degrees signal null. *Magnetic resonance in medicine*. 58:622-630.
43. Balezeau F, Eliat PA, Cayamo AB, Saint-Jalmes H. 2011. Mapping of low flip angles in magnetic resonance. *Physics in medicine and biology*. 56:6635-6647.
44. Sacolick LI, Wiesinger F, Hancu I, Vogel MW. 2010. B1 mapping by Bloch-Siegert shift. *Magnetic resonance in medicine*. 63:1315-1322.
45. Chung S, Kim D, Breton E, Axel L. 2010. Rapid B1+ mapping using a preconditioning RF pulse with TurboFLASH readout. *Magnetic resonance in medicine*. 64:439-446.
46. Voigt T, Nehrke K, Doessel O, Katscher U. 2010. T1 corrected B1 mapping using multi-TR gradient echo sequences. *Magn Reson Med*. 64:725-733.
47. Klein S, Staring M, Murphy K, Viergever MA, Pluim JP. 2010. elastix: a toolbox for intensity-based medical image registration. *IEEE transactions on medical imaging*. 29:196-205.
48. Li Z, Tielbeek JA, Caan MW, Puylaert CA, Ziech ML, Nio CY, Stoker J, van Vliet LJ, Vos FM. 2015. Expiration-phase template-based motion correction of free-breathing abdominal dynamic contrast enhanced MRI. *IEEE transactions on bio-medical engineering*. 62:1215-1225.
49. Klein S, Staring M. 2004. elastix]. Available from: http://elastix.isi.uu.nl/index.php.
50. Calamante F. 2013. Arterial input function in perfusion MRI: a comprehensive review. *Prog Nucl Magn Reson Spectrosc*. 74:1-32.
51. Yankeelov TE, Rooney WD, Huang W, Dyke JP, Li X, Tudorica A, Lee JH, Koutcher JA, Springer CS, Jr. 2005. Evidence for shutter-speed variation in CR bolus-tracking studies of human pathology. *NMR in biomedicine*. 18:173-185.
52. Yankeelov TE, Rooney WD, Li X, Springer CS, Jr. 2003. Variation of the relaxographic "shutter-speed" for transcytolemmal water exchange affects the CR bolus-tracking curve shape. *Magn Reson Med*. 50:1151-1169.
53. Logan J, Fowler JS, Volkow ND, Wolf AP, Dewey SL, Schlyer DJ, MacGregor RR, Hitzemann R, Bendriem B, Gatley SJ, et al. 1990. Graphical analysis of reversible radioligand binding from time-activity measurements applied to [N-11C-methyl]-(-)-cocaine PET studies in human subjects. *J Cereb Blood Flow Metab*. 10:740-747.
54. Peeters F, Annet L, Hermoye L, Van Beers BE. 2004. Inflow correction of hepatic perfusion measurements using T1-weighted, fast gradient-echo, contrast-enhanced MRI. *Magnetic resonance in medicine*. 51:710-717.
55. Ivancevic MK, Zimine I, Montet X, Hyacinthe JN, Lazeyras F, Foxall D, Vallee JP. 2003. Inflow effect correction in fast gradient-echo perfusion imaging. *Magnetic resonance in medicine*. 50:885-891.
56. Roberts C, Little R, Watson Y, Zhao S, Buckley DL, Parker GJ. 2011. The effect of blood inflow and B1-field inhomogeneity on Measurement of the arterial input function in axial 3D spoiled gradient echo dynamic contrast-enhanced MRI. *Magnetic Resonance in Medicine*. 65:108-119.
57. Heilmann M, Kiessling F, Enderlin M, Schad LR. 2006. Determination of pharmacokinetic parameters in DCE MRI: Consequence of nonlinearity between contrast agent concentration and signal intensity. *Invest Radiol*. 41:536-543.
58. Bokacheva L, Rusinek H, Chen Q, Oesingmann N, Prince C, Kaur M, Kramer E, Lee VS. 2007. Quantitative determination of Gd-DTPA concentration in T1-weighted MR renography studies. *Magnetic Resonance in Medicine*. 57:1012-1018.
59. Kim H, Morgan DH. 2017. Semiautomatic Determination of Arterial Input Function in DCE-MRI of the Abdomen. *Journal of Biomedical Engineering and Medical Imaging*. 4:96-104.
60. Parker GJ, Roberts C, Macdonald A, Buonaccorsi GA, Cheung S, Buckley DL, Jackson A, Watson Y, Davies K, Jayson GC. 2006. Experimentally-derived functional form for a population-averaged high-temporal-resolution arterial input function for dynamic contrast-enhanced MRI. *Magn Reson Med*. 56:993-1000.
61. Onxley J, Yoo D, Muradyan N, MacFall J, Brizel D, Craciunescu O. 2012. SU-D-BRB-06: Comprehensive Population-Averaged Arterial Input Function (AIF) for DCE-MRI of Head and Neck Cancer. *Med Phys*. 39:3615-3616.
62. Wang Y, Huang W, Panicek DM, Schwartz LH, Koutcher JA. 2008. Feasibility of using limited-population-based arterial input function for pharmacokinetic modeling of osteosarcoma dynamic contrast-enhanced MRI data. *Magn Reson Med*. 59:1183-1189.
63. Yankeelov TE, Cron GO, Addison CL, Wallace JC, Wilkins RC, Pappas BA, Santyr GE, Gore JC. 2007. Comparison of a reference region model with direct measurement of an AIF in the analysis of DCE-MRI data. *Magn Reson Med*. 57:353-361.
64. Yankeelov TE, DeBusk LM, Billheimer DD, Luci JJ, Lin PC, Price RR, Gore JC. 2006. Repeatability of a reference region model for analysis of murine DCE-MRI data at 7T. *J Magn Reson Imaging*. 24:1140-1147.
65. Yankeelov TE, Luci JJ, Lepage M, Li R, Debusk L, Lin PC, Price RR, Gore JC. 2005. Quantitative pharmacokinetic analysis of DCE-MRI data without an arterial input function: a reference region model. *Magn Reson Imaging*. 23:519-529.
66. Yang C, Karczmar GS, Medved M, Oto A, Zamora M, Stadler WM. 2009. Reproducibility assessment of a multiple reference tissue method for quantitative dynamic contrast enhanced-MRI analysis. *Magn Reson Med*. 61:851-859.
67. Yang C, Karczmar GS, Medved M, Stadler WM. 2007. Multiple reference tissue method for contrast agent arterial input function estimation. *Magn Reson Med*. 58:1266-1275.
68. Kim H. 2018. Modification of population based arterial input function to incorporate individual variation. *Magn Reson Imaging*. 45:66-71
69. Tofts PS. 1997. Modeling tracer kinetics in dynamic Gd-DTPA MR imaging. *Journal of magnetic resonance imaging : JMRI*. 7:91-101.
70. Tofts PS, Brix G, Buckley DL, Evelhoch JL, Henderson E, Knopp MV, Larsson HB, Lee TY, Mayr NA, Parker GJ, Port RE, Taylor J, Weisskoff RM. 1999. Estimating kinetic parameters from dynamic contrast-enhanced T(1)-weighted MRI of a diffusable tracer: standardized quantities and symbols. *J Magn Reson Imaging*. 10:223-232.
71. Li X, Huang W, Yankeelov TE, Tudorica A, Rooney WD, Springer CS, Jr. 2005. Shutter-speed analysis of contrast reagent bolus-tracking data: Preliminary observations in benign and malignant breast disease. *Magn Reson Med*. 53:724-729.
72. Kim S, Quon H, Loevner LA, Rosen MA, Dougherty L, Kilger AM, Glickson JD, Poptani H. 2007. Transcytolemmal water exchange in pharmacokinetic analysis of dynamic contrast-enhanced MRI data in squamous cell carcinoma of the head and neck. *Journal of magnetic resonance imaging : JMRI*. 26:1607-1617.
73. Li X, Priest RA, Woodward WJ, Tagge IJ, Siddiqui F, Huang W, Rooney WD, Beer TM, Garzotto MG, Springer CS, Jr. 2013. Feasibility of shutter-speed DCE-MRI for improved prostate cancer detection. *Magn Reson Med*. 69:171-178.

74. Tofts PS, Kermode AG. 1991. Measurement of the blood-brain barrier permeability and leakage space using dynamic MR imaging. 1. Fundamental concepts. *Magnetic resonance in medicine*. 17:357-367.
75. Pierce LA, 2nd, Elston BF, Clunie DA, Nelson D, Kinahan PE. 2015. A Digital Reference Object to Analyze Calculation Accuracy of PET Standardized Uptake Value. *Radiology*. 277:538-545.
76. Semmineh NB, Stokes AM, Bell LC, Boxerman JL, Quarles CC. 2017. A Population-Based Digital Reference Object (DRO) for Optimizing Dynamic Susceptibility Contrast (DSC)-MRI Methods for Clinical Trials. *Tomography*. 3:41-49.
77. Barboriak DP. 2014. QIBA - Digital Reference Object for Profile DCE-MRI Analysis Software Verification 2]. Available from: https://scholars.duke.edu/display/gra211722.
78. Rohrer M, Bauer H, Mintorovitch J, Requardt M, Weinmann HJ. 2005. Comparison of magnetic properties of MRI contrast media solutions at different magnetic field strengths. *Invest Radiol*. 40:715-724.
79. Morell A, Lennmyr F, Jonsson O, Tovedal T, Pettersson J, Bergquist J, Zemgulis V, Einarsson GM, Thelin S, Ahlstrom H, Bjornerud A. 2015. Influence of blood/tissue differences in contrast agent relaxivity on tracer-based MR perfusion measurements. *MAGMA*. 28:135-147.
80. Laurent S, Elst LV, Muller RN. 2006. Comparative study of the physicochemical properties of six clinical low molecular weight gadolinium contrast agents. *Contrast Media Mol Imaging*. 1:128-137.